LAWRENCE
LIVERMORE
NATIONAL
LABORATORY

LLNL-JRNL-667961

Demonstrating the saturation of stimulated Brillouin scattering by ion acoustic decay using fully kinetic simulations

T. Chapman, B. J. WInjum, S. Brunner, R. L. berger, J. W. Banks

March 2, 2015

Demonstrating the saturation of stimulated Brillouin scattering by ion acoustic decay using fully kinetic simulations

Disclaimer

Demonstrating the saturation of stimulated Brillouin scattering by ion acoustic decay using fully kinetic simulations

T. Chapman,[1, a)] B. J. Winjum,[2] S. Brunner,[3] R. L. Berger,[1] and J. W. Banks[4]
[1)] *Lawrence Livermore National Laboratory, P.O. Box 808, Livermore, CA 94551, USA*
[2)] *Department of Electrical Engineering, University of California Los Angeles, Los Angeles, California 90095, USA*
[3)] *Centre de Recherches en Physique des Plasmas, Association EURATOM-Confédération Suisse, Ecole Polytechnique Fédérale de Lausanne, CRPP-PPB, CH-1015 Lausanne, Switzerland*
[4)] *Department of Mathematical Sciences, Rensselaer Polytechnic Institute, 301 Amos Eaton Hall, Troy, NY 12180, USA*

(Dated: 17 September 2015)

The saturation of stimulated Brillouin scattering (SBS) by the decay to turbulence of the ion acoustic wave (IAW) that participates in the three-wave SBS interaction is demonstrated using a quasi-noiseless one-dimensional numerical solution to the Vlasov-Maxwell system of equations. This simulation technique permits careful examination of the decay process and its role in the complex evolution of SBS. The IAW decay process is shown to be an effective SBS saturation mechanism. In our example, the instantaneous plasma reflectivity saturates at ∼30% and drops to ∼0% as a direct consequence of IAW decay. A contrasting example where the reflectivity is controlled by dephasing due to the nonlinear frequency of the IAW is also discussed.

I. INTRODUCTION

Stimulated Brillouin scattering (SBS) persists as a problematic source of backward-scattered light in indirect-drive inertial confinement fusion (ICF) experiments. In ICF experiments, plasma near the wall of hohlraum targets and in the ablated outer layer of the fuel capsule is observed to produce levels of SBS that are typically energetically weak compared to the total laser energy delivered to the hohlraum. However, when arriving in bursts, this backscattered energy is sufficient to damage the sensitive and expensive optics required at facilities such as the National Ignition Facility (NIF) and remains a central consideration in experimental design[1].

In the SBS process, laser light scatters from and drives ion acoustic waves (IAWs). IAWs are weakly dispersive, permitting coupling between modes with wave numbers that differ greatly and making IAWs susceptible to decay[2]. IAW decay has been observed directly in dedicated Thomson scattering experiments[3,4] and correlated with the saturation of SBS[3]. Numerical studies have identified IAW decay during SBS saturation[5–9], while other work has examined IAW decay in isolation[10–13] and demonstrated the role of electron kinetic effects in IAW nonlinearity[10,11,13,14]. In Ref. 13, the efficient mode-mode coupling of IAWs was found in simulations of both free and continuously driven IAWs to result in a decay process that occurred readily across much of the parameter space of relevance to ICF experiments.

Study of IAW decay has been motivated in part by the potential of this decay process to saturate the SBS instability. The decay of the IAW driven during SBS would naturally act to suppress further scattering of the laser light, thereby limiting the reflectivity (scattered over incident power) of the plasma. The numerical results of prior work[5,7–9,11,13] suggest that IAW decay can indeed lead to a highly turbulent nonlinear state. Due to kinetic effects, the decay process does not conserve energy stored in the field of the IAWs, resulting in particle heating.

In the current work, we investigate the role of IAW decay in SBS saturation using the kinetic code SAPRISTI[14,15], which solves here the collisionless 1D1V (one spatial and one velocity dimension) Vlasov-Maxwell system of equations using a continuum method. Our simulations include the kinetic behavior of electron and ion species, both of which play important roles in the nonlinearity of IAWs. The simulations presented are designed to distinguish the saturation of SBS via IAW decay from other saturation mechanisms, such as depletion of the laser light (or "pump") due to scattering and dephasing due to a nonlinear frequency shift of the IAW. Our simulations demonstrate the effective saturation of SBS by the decay of the primary IAW to subharmonic modes (i.e., modes that do not have wave numbers that are integer multiples of the fundamental). In addition to decay-generated subharmonics, significant IAW harmonic generation[14] is also observed, a process that has been found to be important in reduced models of SBS[16,17] and may influence IAW decay rates[9,12,13].

In our simulations, we seed SBS but not the stimulated Raman scattering (SRS) process (see Appendix for details). Due to the quasi-noiseless simulation technique employed, we do not observe SRS. This approach allows the study of SBS in isolation from the SRS process.

In the following, plasmas will be categorized by the parameter $\alpha = ZT_e/T_i$. This parameter determines the

[a)] email: chapman29@llnl.gov

strength of the ion Landau damping of IAWs in the linear regime (i.e., before significant particle trapping has occurred, which acts to suppress Landau damping). In ICF experiments, laser light interacts with low-Z hohlraum gas fill (He) and capsule ablator (CH, Be, C) materials as well as high-Z hohlraum wall materials (Au, U). Laser pulse lengths are sufficient for electron-ion temperatures to nearly equilibrate until peak power is reached. As a result, plasma conditions vary across $4 \lesssim \alpha \lesssim 100$. IAW decay was found previously[5,13] to behave similarly in both single and multi-ion species plasmas; here, we study a single ion species plasma (He) in regimes characterized by values of α that differ greatly.

Our key findings are summarized as follows: When the decay IAW modes of the fundamental IAW mode that is resonant with the SBS interaction become comparable in amplitude to the fundamental mode, the fundamental mode collapses and a highly turbulent state that is only weakly reflective ensues. The decay process is qualitatively described by a fluid-like decay of the IAW to two daughter IAW modes[2], known as two-ion wave decay, and was observed to be weakened by increasing α in a 1D system[13]. At high α (we show the case $\alpha = 50$) where ion kinetic effects are negligible, ion wave decay is suppressed. In this case, the evolution of the reflectivity is dominated by the dephasing of the driven IAW from the ponderomotive drive of the light waves[7,8,18–22]. This dephasing is due to the trapping-induced nonlinear shift of the IAW frequency away from its linear value, dominated at high α by electron trapping[14].

The paper is organized as follows: The physical motivation behind our choice of plasma parameters is given in Sec. II. In Sec. III A, simulations are presented showing SBS saturation via IAW decay and the resulting particle heating in Sec. III A 2. In Sec. III B, simulations are presented showing SBS saturation by the nonlinearity of the IAW frequency. Finally, in Sec. IV, we discuss our results in the context of relevant prior work.

II. MOTIVATION OF PARAMETERS

Our goal is to demonstrate the role of ion wave decay as a saturation mechanism of SBS independent from other potential saturation mechanisms. To this end, two distinct cases are addressed in this work. The parameters for these cases, labeled set $S1$ and $S2$, are summarized in Table I. Significant prior simulation studies have been accomplished in which IAW decay has been studied explicitly or simply observed to occur; prior work is discussed in the context of the new results presented here in Sec. IV.

We consider a plasma composed of species j with density n_j, charge $Z_j e$, mass m_j, and temperature T_j, where e is the magnitude of the electron charge (note $Z_e \equiv -1$ and $Z_i \equiv Z$ throughout). Subscripts of e and i indicate electron and ion quantities, respectively. The species Debye length is given by $\lambda_{Dj} = v_{tj}/\omega_{pj}$, where

TABLE I. Summary of analytically-determined parameters

Set	ZT_e/T_i	$v_\phi^\dagger/v_{ti}$	$\nu_s^\dagger/\omega_s^L$	$\delta\tilde{\omega}_s^\ddagger$	$I_0^{x=0}$ (W/cm^2)
$S1$	7	3.2	0.060	-0.066	3.5×10^{15}
$S2$	50	6.9	8.2×10^{-3}	0.18	7.0×10^{14}

For both sets, $Z = 2$, $T_e = 2$ keV, $m_i = 4u$ ($^4_2$He), $n_{e0}/n_c = 0.1$, $k_s\lambda_{De} = 0.375$, $L = 100\lambda_0 \approx 200\lambda_s$, $\lambda_0 = 351$ nm, $\omega_1 = \omega_0 - \omega_s^L$, and $I_1^{x=L} = I_0^{x=0}/10^6$.
† Obtained from solving the KDR. Here, $v_\phi = \omega_s^L/k_s$.
‡ $\omega_s^{NL} = \omega_s^L + \delta\omega_s$, where $\delta\omega_s/\omega_s^L = \tilde{\delta\omega}_s\sqrt{e\phi/T_e}$. See Refs. 14, 23, and 24.

$\omega_{pj} = \sqrt{n_j Z_j^2 e^2/(m_j\varepsilon_0)}$ is the species plasma frequency, and $v_{tj} = \sqrt{T_j/m_j}$ the thermal velocity. ε_0 is the permittivity of free space. The complex IAW frequency Ω may be obtained by solving the kinetic dispersion relation (KDR) numerically. For He with Maxwellian species distributions, good analytic approximations are known. The real mode frequency $\omega = \mathrm{Re}(\Omega)$ is,

$$\omega \approx c_i k \left[\frac{1}{(1+k^2\lambda_{De}^2)} + \frac{3}{\alpha}\right]^{1/2}, \tag{1}$$

where $c_i = \sqrt{ZT_e/m_i}$ is the *cold* ion sound speed. The Landau damping may be decomposed into electron and ion contributions $\nu \equiv -\mathrm{Im}(\Omega) \equiv \nu_e + \nu_i$, where,

$$\frac{\nu_e}{\omega} \approx \tilde{\nu}\sqrt{\frac{Zm_e}{m_i}}, \tag{2}$$

$$\frac{\nu_i}{\omega} \approx \tilde{\nu}\alpha^{3/2}\exp\left(-\frac{\alpha}{2}\right), \tag{3}$$

and $\tilde{\nu} = [(\pi/8)/(1+k^2\lambda_{De}^2)^3]^{1/2}$. Note that the quantities k, ω, and ν without subscripts are valid for all linear IAW modes, while the subscript s denotes the specific IAW mode that is resonant in the linear 3-wave SBS interaction. An IAW driven during SBS must satisfy matching conditions in frequency and wave number between itself, the laser light (subscript 0), and scattered light (subscript 1): $\omega_0 = \omega_1 + \omega_s$ and $k_0 = k_1 + k_s$, where here all quantities are real scalars and defined as positive but for $k_1 < 0$ (i.e., the SBS light is scattered backwards).

The laser intensity threshold for SBS is proportional to ν_s/ω_s (see, e.g., Ref. 25) and is highly sensitive to α [see Eq. (3)]. Accordingly, the expected linear SBS response in cases $S1$ and $S2$ may differ substantially for a given laser intensity. In our simulations, the light waves are effectively undamped (apart from at the boundaries) so there is no damping threshold for convective growth. Case $S1$ lies below the threshold for absolute instability. Case $S2$ is slightly above this threshold, but the absolute instability growth rate is small compared to the convective instability growth rate. The convective gain is given by $G_{conv} = 2\Gamma_0^2 L/(c\nu_s)$, where Γ_0 is the SBS growth rate[25]. For $S1$, $G_{conv} = 16$ while for $S2$, $G_{conv} \approx 30$. Discussed subsequently, the applicability of such linear

theory is limited due to the early onset of nonlinearity in our simulations.

In this work, $\Phi = \Phi(x,t)$ is the actual IAW potential, while $\phi = \phi(x,t)$ is the amplitude of the envelope of Φ and typically varies slowly compared to the IAW period. It is often convenient to decompose Φ into Fourier components,

$$\Phi = \sum_l (1/2)\phi_l \exp[i(k_l x - \omega_l t)] + \text{c.c.} \tag{4}$$

While the IAW driven during SBS remains approximately linear, one has $\phi \approx \phi_s$. The traveling potential interacts with resonant particles, i.e. those with velocities close to $v_\phi = \omega_s/k_s$. In addition to Landau damping, resonant particle (kinetic) effects include a nonlinear (amplitude-dependent) frequency shift of the IAW that is a consequence of particles becoming trapped in the wave potential. We differentiate between the linear IAW frequency $\omega_s(\phi \to 0) = \omega_s^L$ and nonlinear frequency ω_s^{NL}, for given wave number k_s, by writing,

$$\omega^{NL} = \omega^L + \delta\omega. \tag{5}$$

Particle trapping will also reduce and in a 1D system may eliminate Landau damping. It is therefore important to the behavior of SBS near threshold. In the simulations presented in the following, species distributions are described by the continuous distribution functions $f_j = f_j(t,x,v)$, where t, x, and v are scalars indicating time, spatial position and velocity, respectively (see Appendix for details). Trapping results initially in a flattening of $\langle f_j \rangle_{\lambda_s}$ in the resonant region of velocity space. This flattening is centered about v_ϕ with a characteristic half-width, $v_{tr,j}$, that may be estimated analytically to good accuracy for wave amplitudes that remain in the perturbative limit[14,23,24]. For electrons under the conditions discussed in this work, resonance occurs in the center of the distribution ($v_\phi/v_{te} \ll 1$), and $v_{tr,e}/v_{te} = 2\sqrt{e\phi/T_e}$; for ions, resonance occurs in the tail of the distribution (here, $v_\phi/v_{ti} > 3$), and $v_{tr,i}/v_{ti} = 2\sqrt{\alpha e\phi/T_e}$. Note that $v_{tr,j}$ is a *half*-width, and trapping occurs within the regions bound by $v_\phi \pm v_{tr,j}$.

For a small-amplitude monochromatic IAW, one has $\delta\omega \propto \sqrt{|\phi|}$ to good accuracy[14,23,24]. Similar to the Landau damping, both electron and ion species contribute to $\delta\omega$, although these contributions are of opposite sign. Both the sign and magnitude of $\delta\omega$ are therefore strongly dependent upon α. An analytic calculation of $\delta\omega$ is possible for both "adiabatic"[14,24] and "sudden"[14,23,24] excitation limits. Here, an adiabatic limit is appropriate for the electrons. The sudden limit is appropriate for the ions in $S1$, while for $S2$, the ion contribution is negligible[14]. Total $\delta\omega_s$ is given in Table I.

The other nonlinear property of IAWs that is important to this study is the decay of the k_s mode. A simple resonant IAW decay model of a mother to two daughter waves is derived in Ref. 2, which gives,

$$\gamma_a = \gamma_b = \frac{c_i}{2}\sqrt{k_a k_b}\left|\frac{e\phi_s}{T_e}\right|, \tag{6}$$

where γ_l is the exponential growth rate of the k_l mode, and the subscripts a and b label the decay (daughter) modes that fulfill $k_s = k_a + k_b$ (and $\omega_s = \omega_a + \omega_b$). This equation is obtained by a simple 3-wave resonant (i.e., without dispersion) IAW decay model and includes no kinetic effects or harmonics of the mother mode[12] and does not capture the dependence of γ_l upon α found in Ref. 13. However, this model qualitatively describes the IAW decay process and provides a useful benchmark for decay rates measured in simulations.

In fluid treatments of IAWs, the quantity $k_s\lambda_{De}$ determines the relative amplitudes of the harmonics of the fundamental IAW[12,14], although such treatments underestimate significantly the strength of harmonic generation present in fully kinetic simulations[13,14]. In $S1$ and $S2$, $k_s\lambda_{De} = 0.375$. The decay mechanism of IAWs was found previously[13] to be weakly if at all sensitive to $k_s\lambda_{De}$.

The minimum set of effective parameters in a collisionless single-ion species plasma is simply $\alpha = ZT_e/T_i$, $k\lambda_{De}$, and Zm_e/m_i for the plasma, and v_{te}/c and n_e/n_c for the light waves, where n_c is the critical density. The cases $S1$ and $S2$ are distinguished primarily by the value of α used in each: $\alpha = 7$ and $\alpha = 50$ (in practice, we vary T_i). In $S1$, the linear Landau damping is significant (of order 5% of the IAW frequency), the IAW decay rate is close to a maximum[13], and the nonlinear frequency shift is negative and of relatively small magnitude[14]. In case $S2$, the linear Landau damping is negligible (less than 1% of the IAW frequency), the IAW decay rate is strongly suppressed[13], while the nonlinear frequency shift is positive and of relatively large magnitude[14]. In the simulations, the initial electron temperature and density are $T_e = 2$ keV and $n_{e0}/n_c = 0.1$, respectively, typical of plasma with significant levels of SBS at the NIF. We do not impose gradients, external fields, or a plasma flow.

In order to study the role of IAW nonlinearity (rather than pump depletion) in SBS saturation, the differing values of α in $S1$ and $S2$ necessitate differing laser intensities, chosen so as to produce similar IAW amplitudes and reflectivities in the two cases. The laser intensity is set to 3.5×10^{15} and 7×10^{14} W/cm^2 in sets $S1$ and $S2$, respectively, with vacuum wave length $\lambda_0 = 351$ nm. The plasma length L is chosen to be $L = 100\lambda_0 \approx 200\lambda_s \approx 3350\lambda_{De}$, where $\lambda_s = 2\pi/k_s$. This length is short enough that the pump does not deplete strongly when undergoing SBS, but large enough that excited IAWs can undergo significant decay before advecting to the boundaries of the system.

III. SIMULATION RESULTS

The simulation setup is summarized in Fig. 1, while a fuller discussion of the simulation technique is given in the Appendix. In both cases, the progression in simulations is as follows: A weak monochromatic electromagnetic seed of intensity $I_1^{x=L}$, frequency ω_1, and wave number k_1 exists throughout the plasma, introduced at

the $x = L$ boundary and propagating in the direction of decreasing x. A laser is introduced at $\omega_{pi}t \sim 100$ and $x = 0$, propagating in the direction of increasing x with intensity $I_0^{x=0}$, frequency ω_0, and wave number k_0.

The light waves drive an IAW via SBS at $(\omega, k) \approx (\omega_s, k_s)$, modifying f_j in the resonant region of velocity and reducing the Landau damping. The seed is amplified via backwards scattering of the laser light across L and consequently I_1 is typically largest near the $x = 0$ boundary. Using the parameters listed in Table I, the simulation duration is approximately $4000/\omega_{pi} \sim 2.4 \times 10^5/\omega_{pe} \sim 140$ ps. The IAW amplitude is largest slightly further from the boundary due to the Krook damping layer (see Appendix) and wave advection. The maximum IAW amplitude grows in tandem with the reflectivity of the plasma, $R \equiv I_1^{x=0}/I_0^{x=0}$, until saturation due to nonlinear processes.

In figures and in the text, normalizations of physical quantities are given explicitly. The exception is the electric field E (either longitudinal or transverse), which is normalized as $\tilde{E} = e\lambda_{De}E/T_e$, where $E_0 = E_0(x,t)$ and $E_1 = E_1(x,t)$ are the transverse electric fields of the pump and scattered light, respectively. $E_x = E_x(x,t)$ is the longitudinal electrostatic field of the plasma waves; $E_x(k) = E_x(k,t)$ denotes the longitudinal spatial Fourier transformation component of E_x with wave number k.

A. Set $S1$: $ZT_e/T_i = 7$, larger ν_s, and smaller $|\delta\omega_s|$

1. Reflectivity and subharmonic growth

This case clearly exhibits the saturation of SBS via IAW decay, with no significant complicating factors. The full plasma parameters for the case discussed in this Section are given in Table I, listed under set $S1$. In Fig. 2, three snapshots in time of the longitudinal electrostatic field (E_x, the IAW) and envelopes of the transverse electromagnetic field intensities (I_0 and I_1) are shown.

In Fig. 2(a), the fields are presented just before the onset of saturation. Between the time snapshots in Figs. 2(a) and 2(b), the k_s IAW mode rapidly decays to its subharmonics, leading to an increasingly turbulent plasma. The moment at which the IAW amplitude (and plasma reflectivity) is lowest is shown in Fig. 2(c). It is apparent in Figs. 2(a-c) that SBS amplification occurs only when E_x is essentially monochromatic. The pump [shown also in Figs. 2(a-c)] is only weakly depleted throughout. Turbulent regions of plasma are minimally if at all reflective.

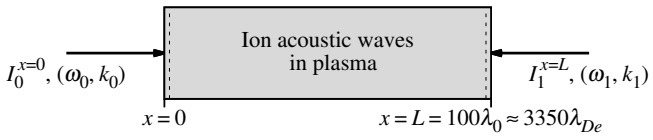

FIG. 1. Basic simulation geometry showing the pump laser (subscript 0) and EM seed wave (subscript 1). Dashed lines indicate the furthest extent of the plasma boundary damping layers (at scale). The EM antennae are within these boundary layers; see Appendix for details.

The plasma reflectivity, R, and evolution of E_x in k-space are shown in Fig. 3(a). R peaks at $\sim$0.35 then falls to $\sim 1 \times 10^{-4}$. The saturation and subsequent crash of R coincide with the onset of IAW turbulence[5,8,9]. After crashing, R begins to grow again; we attribute this recurrence simply to the advection of IAWs and resonant particles out of the simulation box, resetting the system to near its initial quiescent state. The phenomenon of recurrence in SBS has been observed under similar simulation conditions using a PIC code[8], as well as in the study of SRS saturation using Vlasov[26] and PIC[27] codes. The time taken for IAWs and resonant particles to reach the boundary of the system is at most $\tau \sim L/c_i \sim 3500/\omega_{pi}$, in rough agreement with the recurrence period $\tau_{rec} \sim 2300$ observed in Fig. 3. The particle distributions may however retain remnants of their perturbations, even in the absence of any further driving of IAWs; the bulk with $v_{tj} \sim 0$ is also somewhat modified during SBS, and these modifications may propagate slower than c_i.

In Fig. 3(b), the frequency ω_s^{NL} of the IAW k_s mode that is linearly resonant with the pump and seed and the frequency ω_{max} of the largest amplitude IAW mode are shown as deviations from the linear resonant mode frequency, ω_s^L. To obtain the instantaneous frequency of a mode in simulations, the time derivative of the mode phase θ_l is taken: $\omega_l^{NL} = \partial\theta_l/\partial t$, where θ_l is the angle of the complex phasor of $E_x(k_l)$. Early in time, one sees $\omega_{max} = \omega_s^{NL} \approx \omega_s^L$ (i.e., $k_{max} = k_s$), as expected for a regime where the plasma waves remain only weakly nonlinear. Later in time, ω_{max} and ω_s^{NL} begin to diverge. Shown also is the value of $\delta\omega$ given by theory, specified in Table I and using $\langle|\phi|\rangle_L$ for the potential. Good agreement between theory and simulations is not expected, since ϕ varies significantly in space and furthermore the theory assumes a small and monotonically increasing wave amplitude. However, up to the first peak in R, the measured nonlinear frequency shift is negative and qualitatively consistent with theory. At the first peak in R, $\delta\omega$ is of the order of only 1.5%. As a consequence, we do not observe the characteristic beat pattern of a driven nonlinear oscillator present in the case $S2$ (discussed later). A more detailed analysis of the impact of the dephasing of the IAW from the ponderomotive force of the light waves is given in Sec. III B. The mode frequency is ill-defined when the plasma is highly turbulent, and this period in time is omitted from Fig. 3(b).

In order to measure the linear decay mode growth rate, it is necessary to select spatial and temporal windows that are i) small enough in x and t such that the spatio-temporal variations of ϕ_s are small, and ii) large enough such that the resolution in k-space is adequate and short-timescale subharmonic mode amplitude oscillations do not distort the measurement. E_x in the wave frame for

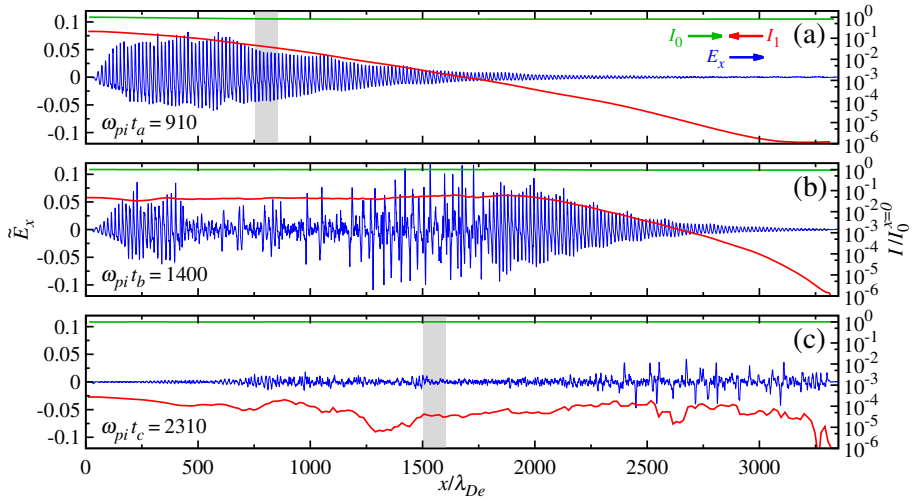

FIG. 2. (Color online) Snapshots in time of the longitudinal electrostatic field (IAW, left linear scale) and transverse electromagnetic fields (laser and scattered light, right logarithmic scale) using parameter set $S1$. The transverse fields are shown as envelope intensities normalized to the input laser intensity, I_0. Turbulent regions in E_x correspond to greatly diminished local growth of I_1 via SBS. Grey boxes indicate sampled regions used in Figs. 7 and 8.

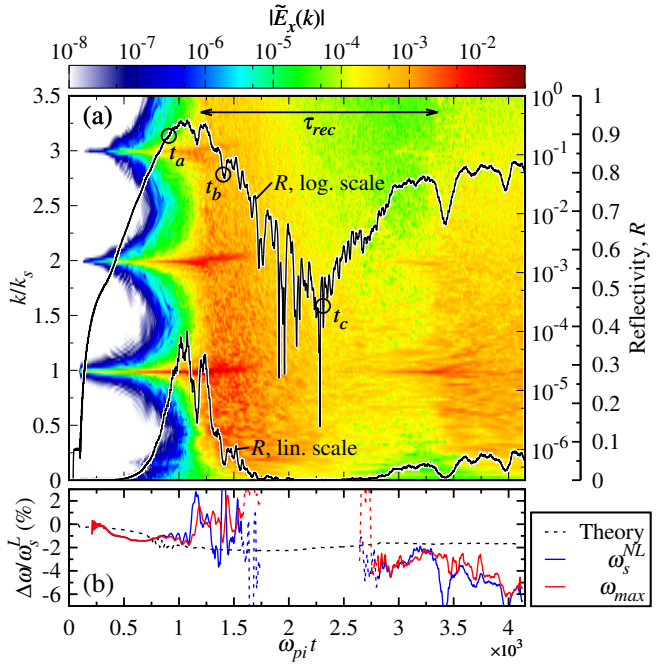

FIG. 3. (Color online) (a) Using set $S1$, the reflectivity of the plasma versus time (right vertical axes, linear and logarithmic scale) and the changing composition of Fourier k modes in the longitudinal field of the IAW (left vertical axis and top color bar). The saturation and fall in reflectivity coincide with the onset of IAW turbulence, while the recurrence period $\tau_{rec} \sim L/c_i$ is determined by the time taken for IAWs to cross the plasma. The circled points $t_{a,b,c}$ correspond to the times shown in Fig. 2(a-c). (b) The deviation from the linear frequency of the resonant mode during SBS, ω_s^L, of i) ω_s^{NL} according to theory given in Table I, ii) ω_s^{NL} from simulation, and iii) the largest amplitude IAW mode, ω_{max}, from simulation.

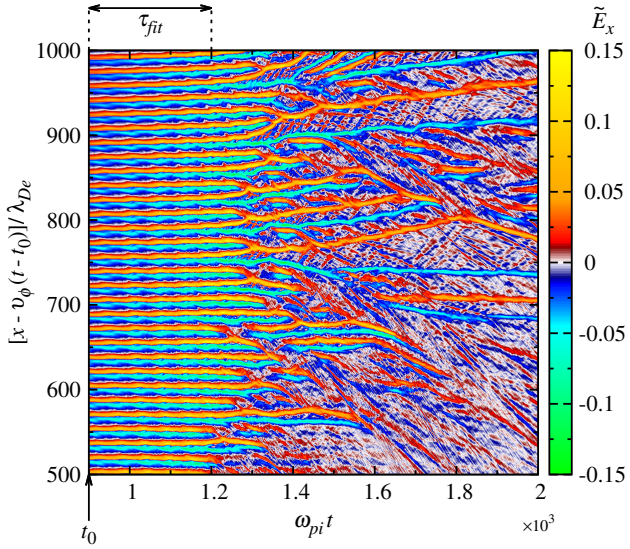

FIG. 4. (Color online) The longitudinal electric field E_x in the wave frame moving at $v_\phi \approx 1.19c_i$, sampled across $\bar{x}|_{t=t_0}/\lambda_{De} = [500, 1000]$ where $\bar{x} = x - v_\phi(t - t_0)$, $\omega_{pi}t_0 = 900$, and v_ϕ is a measured quantity. Period doubling due to the growth of the $k = k_s/2$ mode (half harmonic) is apparent at $\omega_{pi}t \approx 1.3 \times 10^3$, just before the onset of turbulence. Note that there are no backward-propagating modes apparent in the laboratory (stationary) frame.

one such choice of window is shown in Fig. 4. At the onset of turbulence near $\omega_{pi}t \approx 1.3 \times 10^3$, period-doubling due to growth of the half-harmonic of the k_s mode is apparent before the IAW collapses totally. Early in time, the IAW spectrum shown in Fig. 3(a) is dominated by the SBS-driven k_s mode and its harmonics at $k_l = nk_s$, where $n = 1, 2, \ldots$. The subharmonic growth rate, γ_l, of the mode $k_l \neq nk_s$ may be extracted by fitting a linear slope to the logarithm of $|\phi_l|$ (or $|E_x(k_l)|$) in the wave frame. Figure 5(a) shows this fitting process for the k_s mode and its half-harmonic.

Figure 5(b) shows γ_l versus k_l. The regression coefficients of the fits are of order 0.8, indicating that indeed $\phi_l \propto \exp(\gamma_l t)$ for $k_l \neq nk_s$ across the given time window.

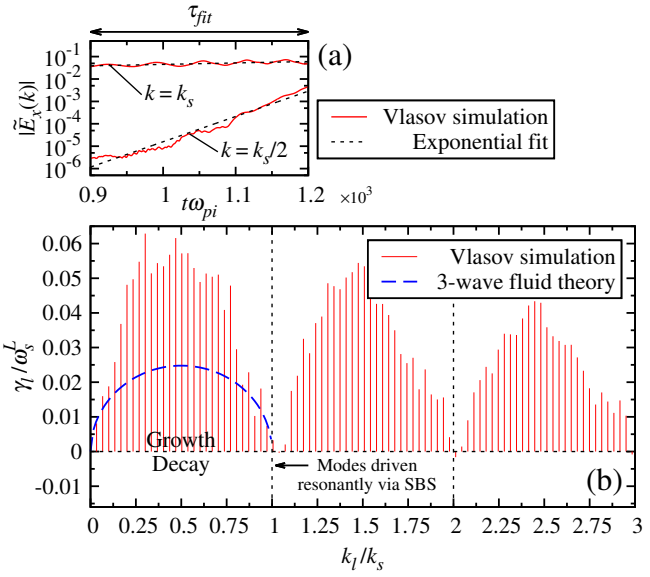

FIG. 5. (Color online) (a) Mode amplitudes versus time for the SBS-driven k_s mode and $k = k_s/2$ decay mode, obtained using set $S1$. Exponential fits are made across τ_{fit} using the moving window defined in Fig. 4. (b) Growth rates γ_l measured using the fitting method shown in the upper figure. Mode growth is fastest near the half-harmonics of the k_s mode, $k_l = (n - 1/2)k_s$. The 3-wave fluid theory is given by Eq. (6) using $\langle e|\phi_s|/T_e\rangle_{\tau_{fit}} = 0.12$.

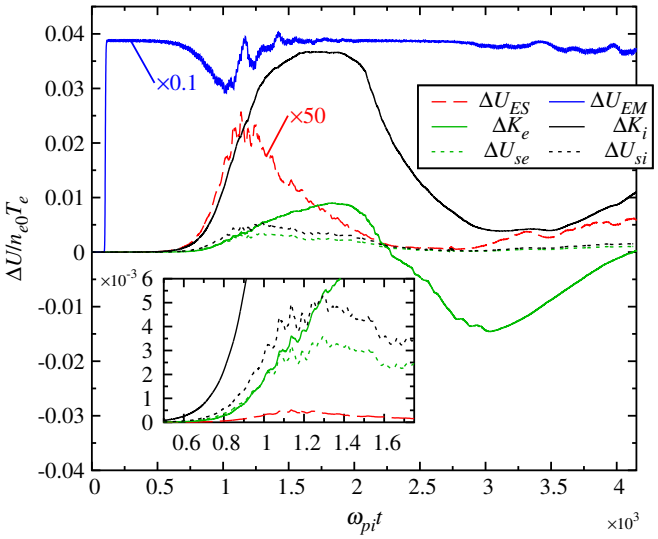

FIG. 6. (Color online) For $S1$, plot of the change in energy density U attributed to the longitudinal electrostatic field (ΔU_{ES}, red line), the transverse electromagnetic field (ΔU_{EM}, blue line), the electron kinetic energy (ΔK_e, green line), and ion kinetic energy (ΔK_i, black line). The jump in U_{EM} at $\omega_{pi}t \sim 100$ is due to the turning on of the laser. The green and black dashed lines are the electron and ion sloshing energies ΔU_{se} and ΔU_{si}, respectively, defined in the text after Eq. (7). Inset, a zoom is shown.

γ_l displays the characteristic features of the two-ion decay process, namely a growth rate that as a function of k_l takes the form of an inverted parabola, is maximal at and symmetric about $k_l = (n - 1/2)k_s$, and is periodic in k_s. The blue dashed line is given by Eq. (6). Growth rates and scalings with both ϕ_s and α were obtained for the decay process in Ref. 13. Despite the difficulties inherent to the measurement of γ_l performed here (in particular, the non-uniform time-varying nature of ϕ_s and corresponding irregular ponderomotive drive strength from SBS), the values of γ_l measured during SBS are in agreement with Ref. 13, where γ_l was found to exceed the predictions of 3-wave fluid theory by a factor of $\sim$3 for $\alpha = 7$ (here, this factor is $\sim$2−3). Note that the IAW subharmonic growth rate is significant, here taking a maximum value of the same order as the linear Landau damping rate (see Table I).

The question of precisely why IAW decay rates often exceed those of a three wave fluid-like model in which the decay is assumed to be exactly resonant (as in Ref. 2) has not been addressed satisfactorily by previous work and remains open. In Ref. 12 it was found in the framework of a fluid (Boltzmann) electron response that decay involving the second harmonic of an IAW mode could be dominant over the decay of the first, characterized by a subharmonic growth rate that scales with $|\phi_2| \propto |\phi_1|^2$ rather than $|\phi_1|$ (here, the subscript denotes the harmonic order; 1 is the 1st harmonic), but clear support for this mechanism was not found in Refs. 9 or 13. In Refs. 13 and 14, it was found that nonlinear electron kinetic effects play an important (perhaps dominant) role in determining the amplitude scaling of $|\phi_{n>1}|$ with $|\phi_1|$, suggesting strongly that *subharmonic* decay rates should also be sensitive to kinetic electron physics. The weak rate at which $|\phi_n|/|\phi_1|$ decreases with n, where all ϕ_n harmonics may act as pumps for subharmonic modes with wave numbers $k_{l\neq n}$, combined with clear evidence of nonlinear electron and ion kinetic effects, presents an unsolved and substantial challenge for theoretical studies.

2. Particle heating

In Fig. 6, the changes in electrostatic (U_{ES}), electromagnetic (U_{EM}), electron kinetic (K_e) and ion kinetic (K_i) energy are shown for $S1$. In the units of Fig. 6, the initial electron and ion kinetic energies are $K_e/(n_{e0}T_e) = 0.5$ and $K_i/(n_{e0}T_e) = 0.5/\alpha = 0.0714$, respectively, where n_{e0} is the *initial* unperturbed electron number density. We are particularly interested here in particle heating via resonant IAWs. However, included in the $K_{e,i}$ is the *sloshing* of the distributions in response to E_x, a process that is reversible in collisionless plasmas and does not contribute to heating[28].

In order to determine the extent (if any) of the particle heating, it is necessary to separate the heating from the sloshing energy. We define for the energy of a spectrum

of IAWs in a Maxwellian distribution[11,28],

$$\frac{U_T}{n_{e0}T_e} = \frac{1}{2}\sum_l k_l^2\lambda_{De}^2\left|\frac{e\phi_l}{T_e}\right|^2 \left.\frac{\partial}{\partial\omega}(\omega\epsilon_L)\right|_{\omega=\omega_l}, \quad (7)$$

where $\epsilon_L = 1+\chi_e+\chi_i$ is the dielectric function and $\epsilon_L(\Omega,k)=0$. It is convenient to use approximate forms of the susceptibilities χ_j,

$$\chi_e \approx \frac{1}{k^2\lambda_{De}^2}, \quad (8)$$

$$\chi_i \approx -\frac{\omega_{pi}^2}{\omega^2}\left(1+3k^2\lambda_{De}^2\frac{\omega_{pi}^2}{\omega^2}\frac{1}{\alpha}\right). \quad (9)$$

Using these expressions to expand the right hand side of Eq. (7) analytically,

$$\frac{\partial}{\partial\omega}(\omega\epsilon_L) \approx 1+\frac{1}{k^2\lambda_D^2}+\frac{\omega_{pi}^2}{\omega^2}\left(1+9k^2\lambda_{De}^2\frac{\omega_{pi}^2}{\omega^2}\frac{1}{\alpha}\right). \quad (10)$$

After substitution of Eq. (10) into Eq. (7), one finds,

$$U_T = U_{ES}+U_{se}+U_{si}, \quad (11)$$

where,

$$\frac{U_{ES}}{n_{e0}T_e} = \frac{1}{2}\sum_l k_l^2\lambda_{De}^2\left|\frac{e\phi_l}{T_e}\right|^2, \quad (12)$$

$$\frac{U_{se}}{n_{e0}T_e} = \frac{1}{2}\sum_l \left|\frac{e\phi_l}{T_e}\right|^2, \quad (13)$$

$$\frac{U_{si}}{n_{e0}T_e} = \frac{1}{2}\sum_l \left(\beta_l+\frac{9}{\alpha}\beta_l^2\right)\left|\frac{e\phi_l}{T_e}\right|^2, \quad (14)$$

for which U_{sj} is the sloshing energy of species j and $\beta_l = (k_l\lambda_{De}\omega_{pi}/\omega_l)^2$. The heating of species j should be given approximately by $\Delta K_j - U_{sj}$, where $\Delta K_j \equiv K_j(t) - K_j(t=0)$ and $K_j = K_j(t) = (1/L)\iint_\Gamma dx\,dv\,(m_j/2)v^2 f_j$ is calculated directly in the simulations. U_{se} and U_{si} are calculated using the analytic expressions given by Eqs. (1), (13), and (14), with ϕ_l taken from simulations.

For a monochromatic IAW, analytically one finds $U_{se} \sim U_{si} \sim U_{ES}/(k^2\lambda_{De}^2)$. However, as the IAW spectrum becomes turbulent, such a relation does not hold, although in general one has $U_{sj} \gg U_{ES}$. If instead of the approximate expressions for χ_j above one uses the value of ϵ_L given by solving the KDR to obtain ϵ_L numerically, one finds for a monochromatic IAW with $k\lambda_{De}=0.375$ and $\alpha=7$ a change in the value of U_{se} of 0.2% and a change in the value of U_{si} of 6%; i.e., the approximate expressions are adequate for our purposes. As resonant particle interactions become more significant, the distributions diverge increasingly from Maxwellian, decreasing the validity of Eqs. (13) and (14); this is discussed shortly.

In Fig. 6 the electron and ion sloshing energies U_{se} and U_{si} are plotted as green and black dashed lines, respectively. In this case, ΔU_{si} diverges from ΔK_i almost from the outset, while $\Delta U_{se} \sim \Delta K_e$ until the onset of turbulence. After the onset of turbulence, it is clear that the change in kinetic energy in the system is dominated not by sloshing, but by what we refer to here as heating. This assertion may additionally be checked for the ions by verifying that the change in kinetic energy occurs primarily in the resonant region rather than in the bulk of the distribution, i.e. $\Delta K_{res} \approx \Delta K_i$, where,

$$K_{res} \approx \frac{1}{L}\int_x dx\,\frac{1}{2}m_i\int_{v>v_-} dv\,v^2 f_i, \quad (15)$$

and $v_- \equiv v_\phi - v_{tr,i}$. The relation $\Delta K_{res} \approx \Delta K_i$ is satisfied to within approximately 5% throughout the simulation. Such a check is not possible for the electrons, since the resonant region encompasses the bulk.

K_i increases from its initial value by ∼50% and $K_{e,i}$ continue to grow long after the reflectivity saturates. It is important to note that the increase in $K_{e,i}$ that occurs after the peak in U_{ES} at $\omega_{pi}t \sim 1.2\times10^3$ in Fig. 6 can *not* be attributed to a simple conversion of U_{ES} to $K_{e,i}$ via the decay of effectively undriven IAWs, since $|\Delta K_{e,i}| \gg |\Delta U_{ES}|$; IAWs are *continuously* driven despite the weak reflectivity during the turbulent phase, and their electrostatic energy is converted to kinetic energy. This finding is consistent with Refs. 11 and 13.

The Krook boundary layers damp the distributions back to being Maxwellian, generally reducing kinetic energy at the edges of the plasma. Kinetic energy is lost from the system primarily via this process. Electron trapping in IAWs serves to flatten the peak of the distribution in velocity space. Electrons then propagate to either boundary (note that generally $|v_\phi \pm v_{tr,e}| \gg v_\phi$, and therefore resonant electrons have a larger spread in velocity than resonant ions and will reach the boundaries sooner) and are damped back to being Maxwellian. This damping of the perturbed distribution results in a value of K_e below that of a quiescent plasma (recall that $K_{e,i}$ are spatially-averaged quantities), apparent in the negative value of ΔK_e shown in Fig. 6. The time taken for the reflectivity to recur, τ_{rec} (introduced in Sec. III A 1), is in agreement with the time taken in Fig. 6 for $\Delta K_{e,i}$ to grow, saturate, and return to zero (and likewise for $f_{e,i}$ to return to a state close to the initial quiescent one); this is discussed further in Sec. IV.

Examples of the ion and electron distributions typical of those during SBS are shown at snapshots in time (and for small samples in x) in Figs. 7 and 8, respectively; the velocity region has been restricted to that resonant with IAWs, and the distribution is shown as a deviation from the initial Maxwellian one. Figs. 7(a) and 8(a) show the particle distributions in a turbulence-free spatial region. The λ_s-periodic nature of the SBS-driven IAW is evident in both species distributions, while the deviation of the distributions from Maxwellian are contained approximately within the regions bound by $v_\phi \pm v_{tr,j}$. Figs. 7(b) and 8(b) show the distributions in a highly turbulent spatial region of the IAW evolution, at which point the

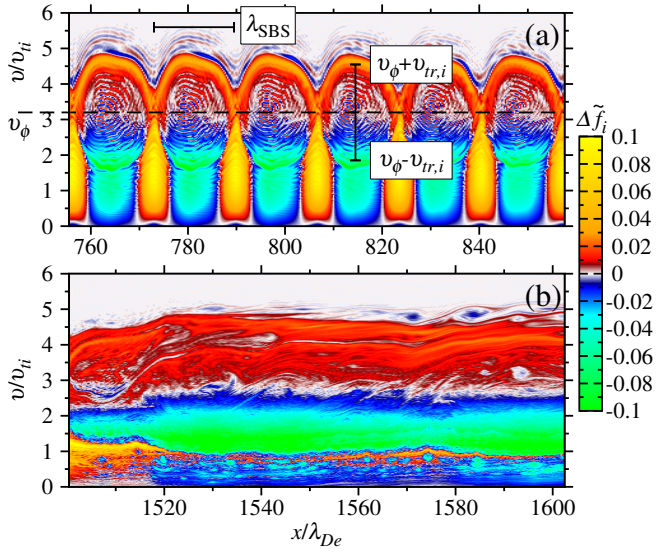

FIG. 7. (Color online) Deviation of the ion distribution, f_i, from Maxwellian, f_M, where $\Delta\tilde{f}_i = [v_{ti}/(Z_i n_{i0})](f_i - f_M)$, shown in the velocity region resonant with IAWs using set $S1$. (a) Spatial region where significant SBS is occurring [sampled region corresponds to grey box of Fig. 2(a)]. (b) Spatial region where turbulence is inhibiting SBS [sampled region corresponds to grey box of Fig. 2(c)]. $v_{tr,i}$ is calculated using $e|\phi_s|/T_e = 0.065$, measured locally.

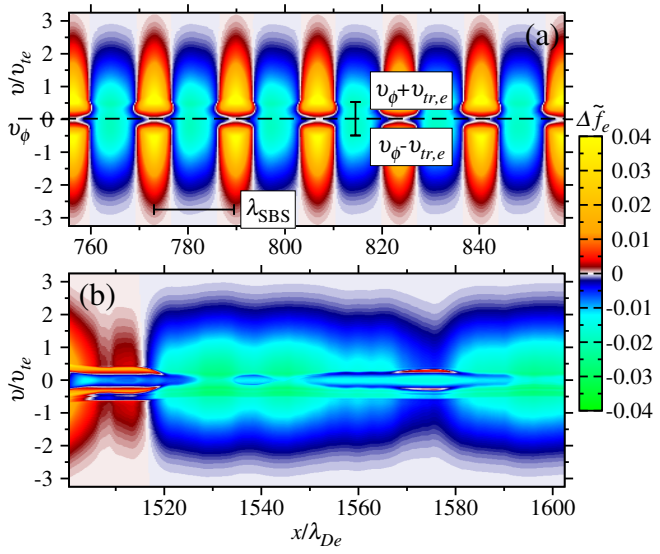

FIG. 8. (Color online) As Fig. 7, but here for the deviation of the electron distribution, $\Delta\tilde{f}_e = (v_{te}/n_{e0})(f_e - f_M)$. $v_{tr,e}$ is calculated using $e|\phi_s|/T_e = 0.065$, measured locally.

distributions show little evidence of a coherent plasma wave.

In Fig. 9(a), $\langle f_i\rangle_L$ is shown. Time-varying estimates of the ion trapping widths $v_{tr,i}^{av}$ and $v_{tr,i}^{max}$ calculated using the average and maximum of ϕ, respectively, are also shown. $\langle f_i\rangle_L$ has a flattened region in velocity that is bounded to reasonable accuracy by $v_\phi \pm v_{tr,i}^{max}$. Using

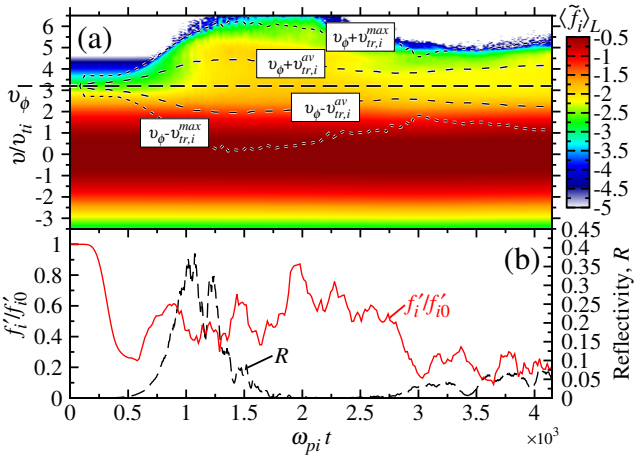

FIG. 9. (Color online) For the case $S1$, (a) $\langle\tilde{f}_i\rangle_L$ with the maximum and averaged ion trapping widths $v_\phi \pm v_{tr,i}$ where $v_{tr,i}^{max} = 2v_{ti}(\alpha e\bar{\phi}/T_e)^{1/2}$ and $v_{tr,i}^{av} = 2v_{ti}(\alpha e\langle|\phi|\rangle_L/T_e)^{1/2}$, respectively, for which $\bar{\phi} = \max(|\phi|)$. ϕ is obtained using the Hilbert transform[14]. (b) The ratio of the time-varying system length-averaged slope of the ion distribution $f_i' = d\langle f_i\rangle_L/dv|_{v_\phi}$ to the initial (Maxwellian) slope $f_{i0}'|_{v_\phi}$. Also shown is the plasma reflectivity, R.

$v_\phi \pm v_{tr,i}^{av}$ underestimates the extent of the flattened region of the distribution.

In linear theory, ion Landau damping is proportional to $df_i/dv|_{v_\phi}$, and while the IAW is very small, standard linear theory (where the distribution is assumed Maxwellian) is valid. While the IAW is quasi-monochromatic and growing, trapped particles undergo phase mixing, suppressing Landau damping in a spatio-temporally varying fashion, and linear theory is not applicable (perhaps beginning as early as $\omega_{pi}t \sim 200$ in $S1$). However, when particle orbits become untrapped after the onset of turbulence, one expects Landau damping to again roughly follow linear theory, albeit with a non-Maxwellian distribution function. In Fig. 9(b), the ratio of $d\langle f_i\rangle_L/dv|_{v_\phi}$ to the slope of the initial (Maxwellian) ion distribution is shown. It is interesting that there is no clear correlation between this ratio and R, suggesting that one can not attribute the suppression of SBS simply to an increase in ion Landau damping due to the formation of a hot tail in f_i; this is discussed in Sec. IV.

B. Set $S2$: $ZT_e/T_i = 50$, smaller ν_s, and larger $|\delta\omega_s|$

1. Reflectivity and frequency detuning

The full plasma parameters for the case discussed in this Section are given in Table I, listed under set $S2$. The plasma reflectivity, R, and evolution of E_x in k-space are shown in Fig. 10(a). This case is dominated by a feature not significant in the $S1$ case: the saturation of SBS by the dephasing of the local IAW from the ponderomotive

force of the beating SBS light waves[7,18–22]. This dephasing is due primarily to the trapping-induced nonlinear frequency shift $\delta\omega$, shown in 10(b), and is addressed in more detail later in this section. In $S2$, v_ϕ/v_{ti} is sufficiently large such that ion kinetic effects are very weak, resulting in a positive value of $\delta\omega$ dictated only by electron trapping. The magnitude of $\delta\omega$ from theory in the perturbative limit is larger for given ϕ_s by a factor of 3 or more than that of case $S1$ (see Table I), and is also of opposite sign.

In Ref. 13, it was found that the IAW subharmonic growth rate decreased sharply for $\alpha \gtrsim 15$ in a 1D system for $|e\phi_s/T_e| \lesssim 0.15$. In Fig. 11, an example of measured γ_l is shown, taken during the first period of strong subharmonic growth with time window $\omega_{pi}\tau_{fit} = [1.4, 1.75] \times 10^3$ in a region of large IAW amplitude ($|e\phi_s/T_e| \sim 0.12$). In the case examined here, while IAW decay mode growth rates are generally weak, local regions where $|e\phi_s/T_e| \gtrsim 0.1$ show values of γ_l similar to the case $S1$. In $S2$, strong spatio-temporal variations in the IAW amplitude result in a system-averaged decay mode growth rate that is weak compared to the case $S1$, and decay saturates before the system becomes strongly turbulent until a second subharmonic growth phase at $\omega_{pi}t \approx 3 \times 10^3$. In local regions of high IAW amplitude in $S2$, γ_l appears to exceed expected values based on Ref. 13; this may be because the pump IAW mode is generally not exactly monochromatic and nonlinear mode frequencies evolve substantially, perhaps facilitating a more resonant driving of subharmonic modes than in Ref. 13.

The growth rates in Fig. 11 appear to lack clear symmetry about $k_l = k_s(n - 1/2)$ over the intervals $k_l = [(n-1)k_s, nk_s]$ present in Fig. 5, displaying a bias to lower k that is apparent in the mode amplitudes shown in Fig. 10. With similar plasma parameters, this feature was not observed for freely-propagating IAWs in a periodic system in Ref. 13. However, a similar effect was observed for instability occurring during SRS in Ref. 26 (i.e., asymmetric sideband growth rates about a carrier wave). We attribute this to difficulties in measuring the strictly linear growth phase of subharmonics in the presence of rapidly varying conditions.

We discuss now the role of the nonlinear frequency shift in saturating SBS in more detail. When the ponderomotive force of the light waves is in phase with the IAW, energy may be locally transferred efficiently from the pump to the scattered light and IAW. As the IAW amplitude grows, the phase of the IAW is shifted by $\delta\omega = \delta\omega(|\phi|)$, and this may lead to a *reduction* in IAW amplitude, strongest when the phase mismatch between oscillator (IAW) and driver (ponderomotive force) is equal to π. Taking the $(m_j/2)v^2$ moment of the Vlasov equation and neglecting the heat flow term $Q = (1/2)\sum_j m_j \int dv\ v^3 \partial f_j/\partial x$, one obtains the local

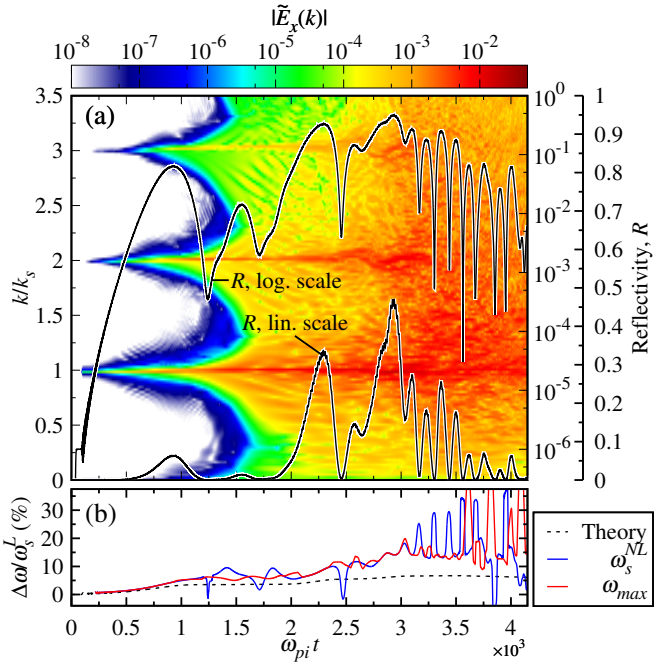

FIG. 10. (Color online) (a) Using set $S2$, the reflectivity of the plasma versus time (right vertical axes, linear and logarithmic scale) and the changing composition of Fourier k modes in the longitudinal field of the IAW (left vertical axis and top color bar). SBS saturation is now due predominantly to the nonlinearity of the IAW frequency. (b) The deviation from the linear frequency of the resonant mode during SBS, ω_s^L, of i) ω_s^{NL} according to theory given in Table I, ii) ω_s^{NL} from simulation, and iii) the largest amplitude IAW mode, ω_{max}, from simulation.

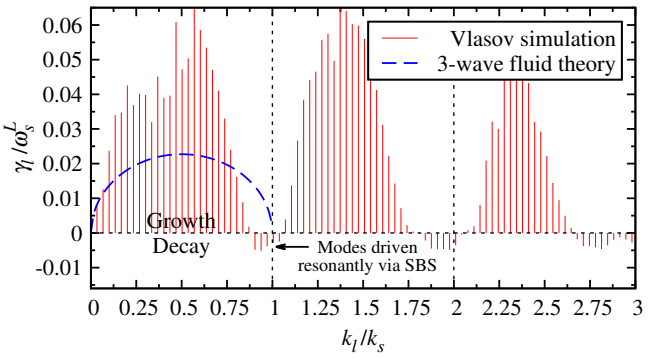

FIG. 11. (Color online) Growth rates γ_l for set $S2$, measured using the fitting method employed in Fig. 5 for time $\omega_{pi}\tau_{fit} = [1400, 1750]$ sampled across $\bar{x}|_{t=t_0}/\lambda_{De} = [500, 1000]$ where $\bar{x} = x - v_\phi(t - t_0)$, $\omega_{pi}t_0 = 1400$, and $v_\phi = 1.02c_i$. The 3-wave fluid theory is given by Eq. (6) using $\langle e\phi/T_e\rangle_{\tau_{fit}} = 0.12$.

power transfer,

$$P = -\sum_j J_j u_{\perp,j} B, \tag{16}$$

where J_j is the charge current, v is the velocity in the longitudinal direction [recall $f_j = f_j(t, x, v)$], $u_{\perp,j}$ is the

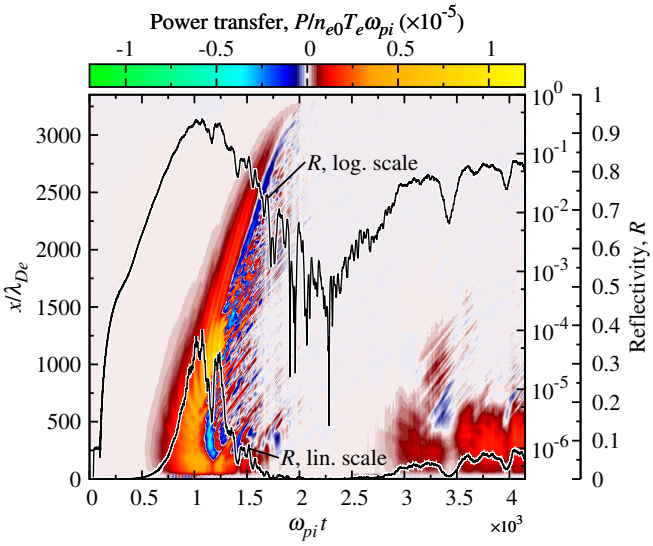

FIG. 12. (Color online) For set $S1$, the evolution of the power transfer, P (left vertical axis and top color bar) defined by Eq. (16) with the plasma reflectivity, R (right vertical axis, linear and logarithmic scale), superimposed. Comparison of P and R indicates saturation of R is *not* caused predominantly in this case by dephasing of the IAW and ponderomotive drive of the light waves.

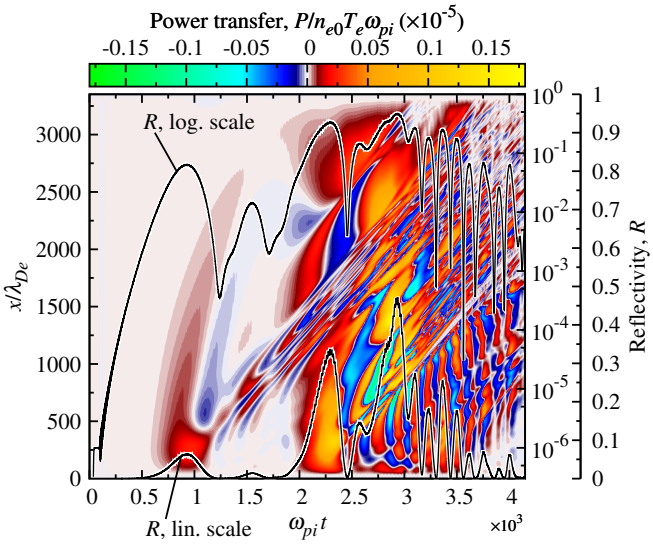

FIG. 13. (Color online) As Fig. 12, but for the case $S2$. Comparison of P and R indicates saturation of R is caused predominantly in this case by dephasing of the IAW and ponderomotive drive of the light waves, and produces rapid oscillations in R late in time.

transverse flow velocity (in the direction of the polarization of the electric field of the laser), and B is the magnetic field of the electromagnetic waves. When $P > 0$, energy is transferred to the IAW as either kinetic or electrostatic energy. After averaging over fast-phase temporal oscillations, it is easy to show that $P \propto \Phi\partial(E_0E_1)/\partial x$, where E_0 and E_1 are the electric field amplitudes of the laser and scattered light, respectively. A similar diagnostic tool was applied successfully to SRS[29,30].

P is plotted for the entire simulated system for cases $S1$ and $S2$ in Figs. 12 and 13, respectively. Averaging of P over λ_s has been performed in order to suppress the sub-λ_s changes of sign of P due to harmonic generation. In Fig. 12, P is positive during the rise of the first peak in the reflectivity R. At the first saturation of R occurring at $\omega_{pi}t \sim 1000$, P is scrambled due to the growth of subharmonic modes, and there is no longer an effective driving of the IAW. The IAW amplitude then collapses, and R continues to fall even when $P \sim 0$. However, in Fig. 13, the oscillations in R are closely correlated with changes of sign in P, apparent even during the rapid oscillations occurring for $\omega_{pi}t \gtrsim 3000$. We conclude that the behavior of R is dominated in case $S2$ by the spatio-temporal variations of $\delta\omega$.

2. The absence of significant particle heating

Electrostatic, electromagnetic, kinetic, and sloshing energies are shown for the case $S2$ in Fig. 14, plotted previously for the case $S1$ in Fig. 6 (the plotted quantities are defined in Sec. III A 2). Despite U_{ES} exceeding the value attained in the case $S1$ by a factor of 2, in the case $S2$ there is no evidence of significant particle heating: throughout the simulation, the kinetic energy of each species is dictated by the sloshing motion, i.e. $\Delta K_j \approx \Delta U_{sj}$. Even when the plasma becomes more strongly turbulent ($\omega_{pi}t \gtrsim 3 \times 10^3$), significant heating occurs of neither electrons nor ions. There are at least two reasons why the heating is so weak in this case: i) The ponderomotive drive from the beating of the light waves is weaker in $S2$ than in $S1$ due to the reduced laser intensity. While this weaker force produces a value of U_{ES} in $S2$ that exceeds that of $S1$ due to the difference in ν_s, it may be that this difference in linear damping has little impact on the nonlinear phase of the simulations. As a consequence, the IAWs would be simply more weakly driven, leading to less heating. ii) There are fewer ions in the resonant region in $S2$ than in $S1$, as shown in Fig. 15 [compare to Fig. 9(a)]. However, this second possibility has no direct effect on electron heating, which is significant in $S1$ but not $S2$.

IV. PRIOR WORK AND DISCUSSION

Previously, simulation-based efforts to understand the nonlinear saturation mechanisms of SBS have been performed using 1D and 2D PIC simulations. In the work of Cohen *et al.*[8,9], a fluid electron model (Boltzmann) was adopted and coupled to a kinetic ion PIC description in a code called BZOHAR. Such an approach allows greatly reduced computational effort, but by design does not describe electron kinetic effects. Because of the differences

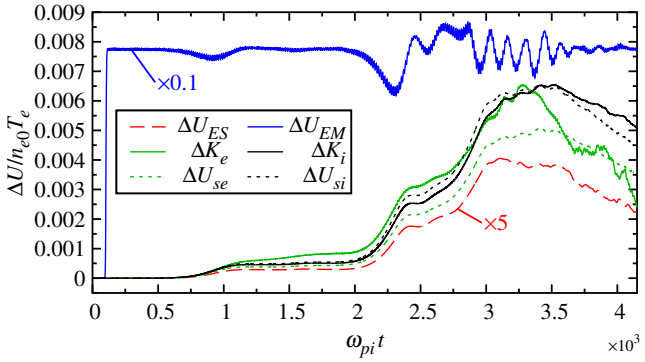

FIG. 14. (Color online) As Fig. 6, but for the case $S2$. Note the differing multiplicative factors applied to ΔU_{ES} in Figs. 6 and 14. In this case, there is little heating and the changes in kinetic energies are dominated by sloshing.

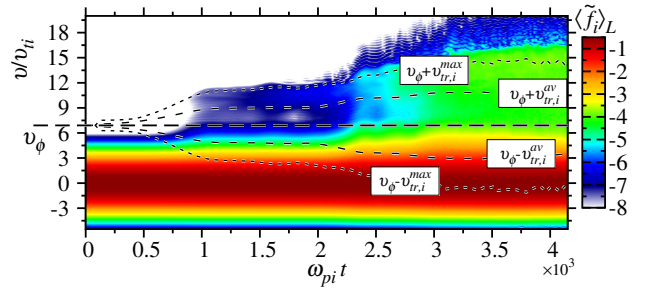

FIG. 15. (Color online) As Fig. 9(a) but now for the case $S2$. The ion Landau damping is not plotted since it remains negligible.

in simulation methodology, timescales, and parameters (in particular, the 1D results of Cohen *et al.* were in a regime of significant pump depletion), quantitative comparisons with the work presented here are difficult. However, some qualitative similarities are clear, such as the presence of significant IAW decay and a correlation of the onset of significant decay with a saturation in SBS. Riconda *et al.*[6] used a similar numerical approach to Cohen *et al.* to study SBS and also observed IAW decay.

It is no surprise that we find electron kinetic effects are important via the trapping-induced nonlinear frequency shift in a collisionless plasma at high α. However, the results of Refs. 10, 11, 13, 14, and the work presented here suggest strongly that electron kinetic effects are important in determining the strength of the IAW mode-mode coupling and therefore harmonic generation and subharmonic decay even at low α. In Refs. 7 and 8, a distinction was drawn between a frequency shift arising due to trapping in a quasi-monochromatic wave and a frequency shift arising due to a quasi-linear modification of the local ion distribution (which may have previously been caused by trapping) during SBS. In Refs. 7 and 8, IAW decay to longer wave lengths occurred and was determined to have an impact upon reflectivity that while substantial was generally weaker than the effect of detuning due to the nonlinearity (and resulting spatial inhomogeneity) of the IAW frequency. The absence of electron kinetic effects in Refs. 7 and 8 that at lower ZT_e/T_i may *reduce* the net frequency shift (in addition to enhancing IAW decay) perhaps played a roll in determining the relative strengths of IAW decay and nonlinear dephasing.

In the results presented here for $S1$ and in previous work[13], it is apparent that when the decay of a quasi-monochromatic IAW results in a state of high IAW turbulence, the field energy crashes. In $S2$, the field energy seemingly does not crash under similar conditions. We attribute this to ion trapping: In $S1$, ion Landau damping is quickly suppressed by trapping as the SBS-resonant fundamental IAW grows early on in the simulation. However, when subharmonic modes reach approximate parity in amplitude with the SBS-resonant fundamental mode, the trapped ion trajectories transition from trapped and periodic to untrapped and chaotic, resulting in a significant loss of wave energy. Furthermore, the de-trapped ions then form a tail with an ion population of higher amplitude than in the initial state that may increase the Landau damping, although as shown at the end of Sec. III A 2, we have not seen evidence of the efficacy of this process. Based on careful PIC simulations, Refs. 7 and 8 conclude that increased ion Landau damping due to the formation of a hot tail is likely not the dominant factor in suppressing recurrence of SBS after saturation.

By performing 1D simulations, we have explicitly neglected IAW decay into modes with a non-zero transverse wave number component. From fluid theory of IAW decay[9,12], it is expected that such decay channels will be faster than modes parallel to the carrier waves, perhaps enhancing IAW decay as a saturation mechanism of SBS compared to 1D systems. However, kinetic effects such as the anisotropic flattening of the species distributions and resulting anisotropic damping may modify such a picture significantly. 2D and 1D PIC simulations were compared by Cohen *et al.*[5,8,9]. The IAW amplitude following saturation in the SBS reflectivity was found to be lower in 2D than in 1D, with IAW decay indeed occurring fastest for non-parallel modes.

As a general remark, we observe that the SBS reflectivity in SAPRISTI appears significantly lower than the reflectivity in PIC simulations published elsewhere. We speculate that this is due to the kinetic electron treatment employed here (which introduces stronger nonlinearity than a fluid electron model) and the noise-induced field fluctuations in PIC simulations that mean less growth is needed in order to reach IAW amplitudes that cause significant SBS. It is apparent from this work and others that there are multiple coexisting and effective mechanisms of saturation of SBS. Which mechanism is dominant will depend upon the laser intensity, but also upon the plasma parameters; further work, using a 2D Vlasov-Maxwell code, would clarify this point.

V. CONCLUSIONS

Using fully-kinetic simulations, we have shown that IAW decay occurs in systems where IAWs are excited by a highly time-varying ponderomotive drive arising from SBS. From these simulations, we have been able to extract for the first time a growth rate of the decay modes that is in agreement with that of freely-propagating IAWs, allowing the unambiguous identification of the decay process. This decay can act as an effective saturation mechanism for SBS in 1D systems, resulting in a crash in IAW amplitude that provokes a loss of plasma reflectivity. The decay occurs more readily in 1D for lower ZT_e/T_i. At $ZT_e/T_i = 50$, dephasing of the driven IAW from the ponderomotive force of the laser and SBS light wave is the dominant saturation mechanism.

ACKNOWLEDGMENTS

We gratefully acknowledge fruitful discussions with Bruce I. Cohen on a range of topics relevant to this work. We are thankful to Bill Arrighi for computer science support essential to the completion of this work. This work was performed under the auspices of the U.S. Department of Energy (DOE) by Lawrence Livermore National Laboratory under Contract DE-AC52-07NA27344 and funded by the Laboratory Research and Development Program at LLNL under project tracking code 15-ERD-038. Benjamin J. Winjum acknowledges support also from the U.S. DOE under Grant Nos. DE-NA0001833 and DE-FC02-04ER54789.

APPENDIX: SIMULATION SETUP

We describe in this Appendix the setup of the numerical simulations presented in this work, summarized in Fig. 1. The interaction of laser light with the plasma is simulated using the kinetic code SAPRISTI, which solves here the collisionless 1D1V Vlasov-Maxwell system of equations. The velocity grid is parallel to the direction of the spatial grid, while a fluid velocity describes motion perpendicular to this axis. Distribution functions for each plasma species (in this case, electrons and one ion species with a physically correct mass ratio) are evolved using a semi-Lagrangian scheme with a time step $\Delta t = 0.1\omega_{pe}^{-1}$, sufficiently small to resolve electron kinetic (wave-particle) effects, with 7 sub-cycled steps for the electromagnetic portion of the calculation. An in-depth discussion of the code is given in Refs. 15 and 14.

In order to resolve $v_{tr,j}$, velocity meshes of 1024 and 2048 points for the electrons and ions, respectively, are chosen, spaced evenly across the ranges $[-8v_{tj}, 8v_{tj}]$ with open boundary conditions. This is sufficient to resolve the complex kinetic phenomena occurring in our simulations across the relevant range of ϕ. A spatial resolution of 64 grid points per λ_s corresponding to $\Delta x \approx 0.26\lambda_{De}$ was chosen, adequate to describe accurately the nonlinear IAW dynamics over the simulated time duration. The total number of spatial grid points across L was 1.28×10^4.

The basic simulation geometry is shown in Fig. 1. The plasma fluctuations at the edge of the simulated system are damped using a Krook operator in the Vlasov equation, ramped up smoothly from an effective damping rate of 0 to a maximum of ω_{pe} across 200 grid points at either edge of the plasma. This Krook operator is chosen to be conservative of particle number but not energy; the species distribution functions are damped back to their initial Maxwellian states, and the boundary layers may be viewed as a thermal bath.

Laser light (assumed linearly polarized) of intensity $I_0^{x=0}$ and frequency $\omega_0 = 2\pi/\lambda_0$ traveling in the direction of increasing x is emitted via an antenna composed of a pair of current sheets near the $x = 0$ boundary. The phasing of the currents ensures that the antenna emits in one direction only. Because the Vlasov-Maxwell solution method employed in SAPRISTI is noiseless to machine precision, the SBS interaction must be seeded in order to occur. This is done via a counter-propagating electromagnetic (EM) seed with intensity $I_1^{x=L} = I_0^{x=0}/10^6$, with a second antenna located near the $x = L$ boundary. The seed frequency ω_1 is chosen by solving simultaneously the wave number and frequency matching conditions, the dispersion relations for the EM waves $\omega_{0,1}^2 = \omega_{pe}^2 + c^2k_{0,1}^2$, and the kinetic dispersion relation for IAWs, where c is the vacuum speed of light; ω_1 differs modestly between $S1$ and $S2$ due to the differing values of α.

During simulations, the seed is launched and allowed to propagate throughout the system before the laser is switched on. Both seed and laser are ramped up in intensity over a time $2 \times 10^3/\omega_{pe}$ (slow enough to maintain quasi-monochromaticity). The boundaries of the system for the EM fields are handled via perfectly matched layers occupying 10 spatial grid points at each boundary. The implementation is based on Refs. 31 and 32. Fourier analysis in space and time of the electric field revealed no significant reflection at the boundaries.

[1] J. L. Kline *et al.*, Phys. Plasmas **20**, 056314 (2013).
[2] S. J. Karttunen, J. N. McMullin, and A. A. Offenberger, Phys. Fluids **24**, 447 (1981).
[3] H. C. Bandulet, C. Labaune, K. Lewis, and S. Depierreux, Phys. Rev. Lett. **93**, 035002 (2004).
[4] C. Niemann, S. H. Glenzer, J. Knight, L. Divol, E. A. Williams, G. Gregori, B. I. Cohen, C. Constantin, D. H. Froula, D. S. Montgomery, and R. P. Johnson, Phys. Rev. Lett. **93**, 045004 (2004).
[5] B. I. Cohen, B. F. Lasinski, A. B. Langdon, and E. A. Williams, Phys. Plasmas **4**, 956 (1997).
[6] C. Riconda, S. Hüller, J. Myatt, and D. Pesme, Phys. Scr., T **T84**, 217 (2000).
[7] L. Divol, B. I. Cohen, E. A. Williams, A. B. Langdon, and B. F. Lasinski, Phys. Plasmas **10**, 3728 (2003).
[8] B. I. Cohen, L. Divol, A. B. Langdon, and E. A. Williams, Phys. Plasmas **12**, 052703 (2005).
[9] B. I. Cohen, E. A. Williams, R. L. Berger, D. Pesme, and C. Riconda, Phys. Plasmas **16**, 032701 (2009), erratum: Phys. Plasmas **16**, 089902 (2009).

[10]C. Riconda, A. Heron, D. Pesme, S. Hüller, V. T. Tikhonchuk, and F. Detering, Phys. Rev. Lett. **94**, 055003 (2005).
[11]C. Riconda, A. Heron, D. Pesme, S. Huller, V. T. Tikhonchuk, and F. Detering, Phys. Plasmas **12**, 112308 (2005).
[12]D. Pesme, C. Riconda, and V. T. Tikhonchuk, Phys. Plasmas **12**, 092101 (2005), erratum: Phys. Plasmas **16**, 089903 (2009).
[13]T. Chapman, S. Brunner, J. W. Banks, R. L. Berger, B. I. Cohen, and E. A. Williams, Phys. Plasmas **21**, 042107 (2014).
[14]R. L. Berger, S. Brunner, T. Chapman, L. Divol, C. H. Still, and E. J. Valeo, Phys. Plasmas **20**, 032107 (2013).
[15]S. Brunner, E. J. Valeo, C. H. Still, R. L. Berger, D. J. Strozzi, E. A. Williams, and J. A. F. Hittinger, Lawrence Livermore National Laboratory Technical Report No. LLNL-SM-409451 (2008).
[16]W. Rozmus, M. Casanova, D. Pesme, A. Heron, and J. Adam, Phys. Fluids. **4**, 576 (1992).
[17]S. Hüller, P. E. Masson-Laborde, D. Pesme, M. Casanova, F. Detering, and A. Maximov, Phys. Plasmas **13**, 022703 (2006).
[18]C. E. Clayton, C. Joshi, and F. F. Chen, Phys. Rev. Lett. **51**, 1656 (1983).
[19]R. E. Giacone and H. X. Vu, Phys. Plasmas **5**, 1455 (1998).
[20]H. X. Vu, D. F. DuBois, and B. Bezzerides, Phys. Plasmas **14**, 012702 (2007).
[21]D. H. Froula, L. Divol, A. A. Offenberger, N. Meezan, T. Ao, G. Gregori, C. Niemann, D. Price, C. A. Smith, and S. H. Glenzer, Phys. Rev. Lett. **93**, 035001 (2004).
[22]E. A. Williams, B. I. Cohen, L. Divol, M. R. Dorr, J. A. Hittinger, D. E. Hinkel, A. B. Langdon, R. K. Kirkwood, D. H. Froula, and S. H. Glenzer, Phys. Plasmas **11**, 231 (2004).
[23]G. J. Morales and T. M. O'Neil, Phys. Rev. Lett. **28**, 417 (1972).
[24]R. L. Dewar, Phys. Fluids **15**, 712 (1972).
[25]D. W. Forslund, J. M. Kindel, and E. L. Lindman, Phys. Fluids **18**, 1002 (1975).
[26]S. Brunner and E. J. Valeo, Phys. Rev. Lett. **93**, 145003 (2004).
[27]B. J. Winjum, J. E. Fahlen, F. S. Tsung, and W. B. Mori, Phys. Rev. E **81**, 045401 (2010).
[28]T. Stix, *Waves in Plasmas* (American Institute of Physics, Woodbury, NY, 1992) Chap. II: Energy flow and accessibility.
[29]B. J. Winjum, Ph.D. thesis, Chapter 2, University of California Los Angeles (2010).
[30]I. N. Ellis, D. J. Strozzi, B. J. Winjum, F. S. Tsung, T. Grismayer, W. B. Mori, J. E. Fahlen, and E. A. Williams, Phys. Plasmas **19**, 112704 (2012).
[31]J.-P. Berenger, J. Comp. Phys. **114**, 185 (1994).
[32]S. Gedney, IEEE Trans. Antennas Propag. **44**, 1630 (1996).